Nonlinear frequency conversion of nondiffracting modes via nondegenerate four-wave mixing in atomic vapor

Onkar N. Verma * and Niti Kant
Department of Physics, University of Allahabad, Prayagraj-211002, Uttar Pradesh, India

(Received 11 January 2024; accepted 29 February 2024; published 13 March 2024)

We investigate the nonlinear frequency conversion of nondiffracting optical modes via a nondegenerate four-wave mixing (FWM) process in rubidium vapor. In this process, two strong control fields and a weak probe field mutually interact via a four-level double-Λ type atomic system to produce a low frequency weak Stokes field which is a phase conjugate to probe. We show that any arbitrary mode such as Airy, Bessel, Mathieu, and Weber beams encoded initially in the spatial envelope of the probe field are efficiently transferred to the FWM Stokes field by satisfying the phase-matching condition. Interestingly, we found that the transmitted intensity profiles of the Stokes beam are identical to that of the probe beam, while the phase profile is complementary. The phase conjugation property of output beams is revealed by interfering them with a copropagating plane wave. We further found the fidelity in terms of structural similarity between two transmitted modes of about 99%, which substantiates the high efficiency of the FWM process. The efficient transfer and frequency conversion of such diffraction-free beams may have potential applications in nonlinear optical and quantum technologies.

DOI: 10.1103/PhysRevA.109.033515

I. INTRODUCTION

The nonlinear frequency conversion of electromagnetic radiation has received great attention recently due to its broad range of applications in the development of optical and quantum technologies [1–4]. For example, such conversion is often required in the functioning of an all-optical integrated device whose individual components operate at certain specific frequencies. To achieve this, nonlinear processes such as sum- or different-frequency generation and four-wave mixing (FWM) techniques have been explored in various nonlinear media such as crystals and atomic vapor [5]. Various frequency up- and down-conversion processes have been developed to generate or detect radiation with frequency ranging from extreme-ultraviolet to far-infrared spectrum [6–8]. The frequency conversion of multimode images is also crucial due to its applications in nonlinear imaging and quantum information processing. Utilizing a stimulated down-conversion process in a nonlinear crystal, Ribeiro *et al.* have theoretically proposed [9] and experimentally demonstrated [10] the transfer of a transverse intensity profile from a pump field to a down-converted idler field. However, the conversion efficiency is low in crystal media and a high-intensity laser or a resonant cavity is often required to increase efficiency. In order to solve the problem of low conversion efficiency, an atomic ensemble is used in various multilevel configurations. An atomic ensemble is a good candidate for studying the generation, propagation, and manipulation of optical beams. This is because its absorptive and dispersive properties are easily controlled by atomic coherence. Ding *et al.* reported a frequency up-conversion process based on FWM to transfer an image from infrared field to visible light using atomic vapor [11]. The transfer of orbital angular momentum (OAM) states of an optical vortex beam from one frequency to another frequency light has been studied using an FWM process in atomic vapor [12,13].

Using a nondegenerate FWM process, Tabosa *et al.* [14] reported experimentally the transfer of OAM from a vortex beam to another oscillating at a different frequency via optical pumping in a cold cesium atomic system. Akulshin *et al.* [15] have suggested a technique to transfer OAM from an incident laser beam to a newly generated optical beam in a ladder-type atomic system. They have further analyzed the transverse intensity and phase profiles of the forward-directed collimated blue and near-IR light using self-interference and astigmatic transformation techniques. In another work, Akulshin *et al.* [16] reported how the orientation of the Rb cell can significantly affect the intensity and spectral characteristics of both the frequency up- and down-converted fields generated by nonlinear processes in Rb vapor. They found that the process of velocity-insensitive two-photon excitation is crucial to understand the coherent blue and mid-IR light enhancements. Chopinaud *et al.* [17] have reported the OAM conversion from a red optical vortex to a blue one with topological charge ranging from -30 to $+30$ in a rubidium atomic vapor. Prajapati *et al.* [18] proposed theoretically and verified experimentally the generation of the collimated blue light in ^{85}Rb vapor using two resonant laser fields exciting atoms into the $5D_{3/2}$ state via an intermediate state $5P_{1/2}$ or $5P_{3/2}$. They have compared the blue light generation for different values of frequency detunings, powers, and polarizations of the pump lasers in two D-line transitions of ^{85}Rb atoms. Their results show that the blue light emission is higher for the D_1 transition as compared to the D_2 transition for similar conditions. Mallick *et al.* [19] discussed a scheme to transfer the OAM from an externally

*onkarnath15verma@gmail.com

applied Laguerre-Gaussian beam to a new frequency FWM field in a homogeneously broadened ^{85}Rb atomic system in a diamond-type configuration. In this case, it is shown how phase singularities of the input vortex beams are mapped onto atomic coherence in a transverse plane, which leads to transfer of OAM to the FWM field. Recently, Qiu *et al.* [20] proposed a scheme to transfer and manipulate the helical phase wavefront of a vortex beam via space-dependent FWM in sodium vapor consisting of four-level atoms. They found that the FWM field can be significantly enhanced and its dynamical phase twist can be completely suppressed by suitably choosing the intensity and detuning of the control field. Yu *et al.* [21] investigated a scheme to control the helical phase wavefront of the FWM beam using two control fields in a six-level tripod atomic system. It is shown that the helical phase-front of the transferred vortex FWM beam can be controlled or suppressed by varying the intensities of two control fields and the detuning of the probe field.

The process of FWM is a well-established nonlinear phenomenon that essentially depends on high intensities of external laser fields [5]. In this process, three laser fields coherently interact with medium to generate a fourth field with a different frequency. The transverse profile of these laser fields and their propagation dynamics strongly affect the efficiency of FWM processes [22,23]. This is because a laser beam experiences a natural paraxial spreading due to diffraction while propagating in free space or medium. This eventually results in a severe distortion of the laser beam profile and causes loss of information in the course of propagation. Further, this beam distortion also degrades the efficiency of the FWM process. To sustain the efficiency, various techniques have been developed to eliminate the distortion due to diffraction [24]. Shpaisman *et al.* [25] have proposed an electromagnetically induced waveguiding mechanism to control the diffraction of a Gaussian probe beam in both single Λ-type and closed-loop double-Λ configurations. In the double-Λ system, the lower Λ-system acts as a waveguide to induce a spatial confinement to laser beams in the upper Λ-system, which undergoes diffraction in the absence of a waveguiding system. They have further shown the frequency conversion between the fields via FWM in the closed-loop double-Λ system. They found that when the upper Λ-system initially interacts with only a single laser beam, the loop is completed by a newly generated anti-Stokes field at the FWM frequency. Their results show that both the applied probe and generated anti-Stokes fields exhibit electromagnetically induced waveguiding and are spatially confined for several diffraction lengths. This waveguiding effect is strongly phase sensitive as it derives from the phase-dependent effective third-order susceptibility of the closed-loop double-Λ system.

In order to escape the diffraction, one can use a class of nondiffracting spatial modes which are exact solutions of the Helmholtz equation (HE) in different coordinate systems. These solutions include Airy [26–28], Bessel [29,30], Mathieu [31,32], and Weber beams [33,34]. They possess several properties such as diffraction-free propagation, self-healing, and self-acceleration in the transverse direction. In the case of diffraction-free propagation, the beam preserves its shape and size while traversing through free space or medium. By their self-healing nature, these beams can reconstruct their original form after being disturbed by smaller objects. The self-acceleration quality is associated with an Airy beam where it experiences a constant acceleration in the transverse plane during propagation. Recently, Wei *et al.* have experimentally demonstrated the generation of Airy beams based on the FWM process in a rubidium atomic vapor [35]. These unique properties make the Airy beam extremely useful for a variety of applications such as particle clearing [36], generation of curved plasma [37], light-sheet microscopy [38], and spatiotemporal light bullets [39]. In this paper, we introduce a scheme to show the transfer and frequency conversion of these nondiffracting beams via the nonlinear FWM process in an atomic vapor.

The paper is organized as follows. In Sec. II A, we introduce our theoretical model for a closed-loop four-level double-Λ system and apply semiclassical theory to describe light-matter interaction. In Sec. II B, we use the density matrix approach to describe dynamics of the atomic system and derive analytical expressions for linear and nonlinear response of the medium under steady-state condition. In Sec. II C, we use the Maxwell-Schrödinger equation to observe the spatial evolutions of probe and FWM fields within paraxial approximation. In Sec. III, we present our numerical results for transfer and frequency conversion of various nondiffracting modes from a probe field to a frequency-converted Stokes field in the FWM process. Section IV provides a brief summary of our results.

II. THEORETICAL FORMULATION

A. Model system

We consider an ensemble of lifetime-broadened ^{87}Rb cold atoms. Each atom is modeled as a four-level system in a double-Λ configuration as depicted in Fig. 1. The electric dipole-allowed transitions $|3\rangle \leftrightarrow |1\rangle$ and $|4\rangle \leftrightarrow |2\rangle$ are coupled by two strong control fields of Rabi frequencies G_{c1} and G_{c2}, respectively. The remaining two transitions $|4\rangle \leftrightarrow |1\rangle$ and $|3\rangle \leftrightarrow |2\rangle$ are driven by a weak probe and newly borne Stokes fields having Rabi frequencies g_p and g_s, respectively. The generic energy level scheme for FWM can be realized in the magnetic sublevels of ^{87}Rb with two ground states assigned as $|1\rangle = |5S_{1/2}, F = 1, m_F = -1\rangle$ and $|2\rangle = |5S_{1/2}, F = 2, m_F = -2\rangle$ and two excited states assigned as $|3\rangle = |5P_{1/2}, F' = 2, m'_F = -1\rangle$ and $|4\rangle = |5P_{3/2}, F' = 2, m'_F = -2\rangle$ [35,40]. The electric fields associated with four optical beams are defined as

$$\vec{E}_j(\vec{r}, t) = \hat{e}_j \mathcal{E}_j(\vec{r})\, e^{-i(\omega_j t - \vec{k}_j \cdot \vec{r})} + \text{c.c.}, \tag{1}$$

where $\mathcal{E}_j(\vec{r})$ are the slowing varying envelopes, $\hat{e}_j$ the unit polarization vectors, ω_i the laser field frequencies, and k_j the wave numbers of fields. The index $j \in \{p, s, c1, c2\}$ denotes the probe, Stokes, and control fields. The Hamiltonian of the atom-field system in electric dipole and rotating-wave approximations is given by

$$\begin{aligned}\hat{H}/\hbar = {} & \omega_1 |1\rangle\langle 1| + \omega_2 |2\rangle\langle 2| + \omega_3 |3\rangle\langle 3| + \omega_4 |4\rangle\langle 4| \\ & - g_p e^{-i\omega_p t} |4\rangle\langle 1| - g_s e^{-i\omega_s t} |3\rangle\langle 2| - G_{c1} e^{-i\omega_{c1} t} |4\rangle\langle 2| \\ & - G_{c2} e^{-i\omega_{c2} t} |3\rangle\langle 1| + \text{H.c.},\end{aligned} \tag{2}$$

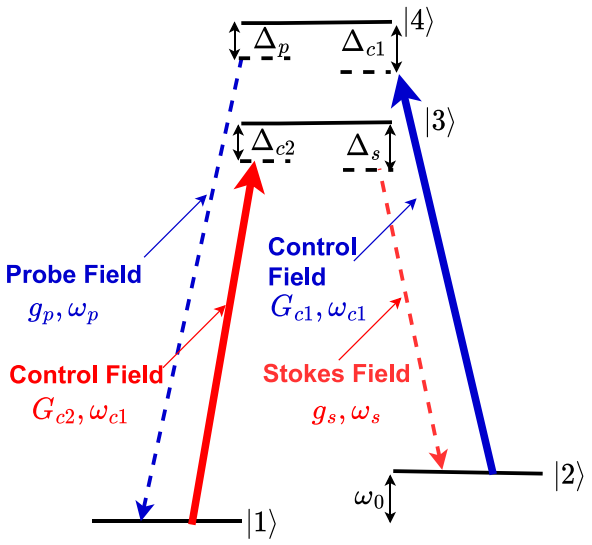

FIG. 1. Four-wave mixing in a closed-loop four-level double-Λ type atomic system. In the first Λ system, a probe field and a control field of Rabi frequencies g_p and G_{c1} drive the transitions $|4\rangle \leftrightarrow |1\rangle$ and $|4\rangle \leftrightarrow |2\rangle$, respectively. The second Λ system is created by the FWM generated Stokes field and another control field of Rabi frequencies g_s and G_{c2} interacting with transitions $|3\rangle \leftrightarrow |2\rangle$ and $|3\rangle \leftrightarrow |1\rangle$, respectively. The angular frequencies and single-photon detunings of the four fields are denoted by ω_i and Δ_i. The ground state frequency splitting is denoted by ω_0.

where $\hbar\omega_j$ is the energy of the corresponding atomic level $|j\rangle$. The Rabi frequencies of four fields are defined as $g_p = \vec{d}_{41} \cdot \hat{e}_p \mathcal{E}_p e^{i\vec{k}_p\cdot\vec{r}}/\hbar$, $g_s = \vec{d}_{32} \cdot \hat{e}_s \mathcal{E}_s e^{i\vec{k}_s\cdot\vec{r}}/\hbar$ and $G_{c1} = \vec{d}_{31} \cdot \hat{e}_{c1} \mathcal{E}_{c1} e^{i\vec{k}_{c1}\cdot\vec{r}}/\hbar$, $G_{c2} = \vec{d}_{42} \cdot \hat{e}_p \mathcal{E}_{c2} e^{i\vec{k}_{c2}\cdot\vec{r}}/\hbar$. Here, d_{jk} are the dipole moments of respective transition $|j\rangle \leftrightarrow \langle k|$ ($j \in \{3, 4\}, k \in \{1, 2\}$).

B. Atom dynamics

The equation of motion of atoms can be derived using the standard density matrix approach,

$$\frac{\partial \rho}{\partial t} = -\frac{i}{\hbar}[\hat{H}, \rho] + \mathcal{L}\rho, \tag{3}$$

where $\mathcal{L}\rho$ is Lindblad operator which describes population and coherence decay. On substituting the Hamiltonian of Eq. (2) into Eq. (3), we get equations of motion for the density matrix elements. The resulting 16 equations have explicit time dependence which can be removed by introducing suitable transformations and ensuring energy conservation condition $\omega_{c1} + \omega_{c2} = \omega_p + \omega_s$ for the FWM process [13]. Now in order to solve these time-independent equations analytically, we find out perturbative solutions to the density matrix elements under steady-state condition ($\partial\sigma/\partial t = 0$). For this, we assume that the probe and Stokes fields are weak enough as compared with control fields so that they can be treated as a perturbation to the system in linear order. Thus, we calculated the atomic coherences σ_{41} and σ_{32} to first order in probe and Stokes fields while all orders in control fields as follows:

$$\sigma_{41} = \alpha_p g_p + \beta_p g_s^* \tag{4a}$$

$$\sigma_{32} = \alpha_s g_s + \beta_s g_p^*, \tag{4b}$$

where the coefficients α_i and β_i are listed in the Appendix. The above two atomic coherences are used to obtain the polarization of the medium for probe ($\vec{P}_p$) and Stokes ($\vec{P}_s$) fields oscillating at frequencies ω_p and ω_s as

$$\vec{P}_p(\omega_p) = \mathcal{N}(\vec{d}_{14}\sigma_{41}e^{-i\omega_p t} + \text{c.c.}) \tag{5a}$$

$$\vec{P}_s(\omega_s) = \mathcal{N}(\vec{d}_{23}\sigma_{32}e^{-i\omega_s t} + \text{c.c.}), \tag{5b}$$

with respective amplitudes $\mathcal{P}_p(\omega_p) = \mathcal{N}d_{14}\sigma_{41}$ and $\mathcal{P}_s(\omega_s) = \mathcal{N}d_{23}\sigma_{32}$. Here, $\mathcal{N}$ is the atomic density of the medium. After substituting expressions for σ_{41} and σ_{32} from Eqs. (4) along with Rabi frequencies for four fields, we can express the polarizations of two fields as a sum of two parts: (1) linear polarization oscillating at frequency ω_i and (2) nonlinear polarization oscillating at frequency $\omega_{c1} + \omega_{c2} - \omega_i$ ($i \in \{p, s\}$) as follows:

$$\mathcal{P}_p(\omega_p) = \chi_{11}(\omega_p)\mathcal{E}_p e^{i\vec{k}_p\cdot\vec{r}} + \chi_{12}(\omega_{c1} + \omega_{c2} - \omega_s) \times \mathcal{E}_s^* e^{i(\vec{k}_{c1}+\vec{k}_{c2}-\vec{k}_s)\cdot\vec{r}} \tag{6a}$$

$$\mathcal{P}_s(\omega_s) = \chi_{22}(\omega_s)\mathcal{E}_s e^{i\vec{k}_s\cdot\vec{r}} + \chi_{21}(\omega_{c1} + \omega_{c2} - \omega_p) \times \mathcal{E}_p^* e^{i(\vec{k}_{c1}+\vec{k}_{c2}-\vec{k}_p)\cdot\vec{r}}, \tag{6b}$$

where χ_{ij} is the complex susceptibility of the atomic medium [41]. The first term χ_{ii} ($\propto \alpha_{p,s}$) describes the linear susceptibility whose real and imaginary parts are respectively responsible for dispersion and absorption of both fields inside the medium. The second term χ_{ij} ($\propto \beta_{p,s}$) represents χ^3-type nonlinear susceptibility and describes the FWM parametric process. In a parametric process an atom is driven from one ground state to another ground state and back to the initial state. Consequently, two photons from control fields are converted into two photons of probe and Stokes fields with frequencies (wave vectors) ω_p (k_p) and ω_s (k_c). Thus, this cross polarization acts as a source term in the propagation equations and enables efficient energy transfer between light fields provided the phase-matching condition ($\Delta\vec{k} = 0$) is satisfied. Here, $\Delta\vec{k}$ is the geometric phase mismatch $\Delta\vec{k} = \vec{k}_{c1} + \vec{k}_{c2} - \vec{k}_p - \vec{k}_s$. It is also important to note that even though there is no Stokes field ($\mathcal{E}_s = 0$) at the input, Eq. (6b) implies that there exists a nonzero term due to nonlinear polarization at frequency ω_s, i.e., $\mathcal{P}_s(\omega_s) = \chi_{21}\mathcal{E}_p^*$. This simply implies that the nonlinear interaction of the optical fields leads to the generation of a Stokes field provided the four-photon resonance condition is satisfied. Further, it is interesting to note here that the polarization $\mathcal{P}_s(\omega_s)$ is proportional to the complex conjugate of the probe ($\mathcal{E}_p^*$) and thus, the generated Stokes wave would be a phase conjugate to the probe beam. Now, in order to see the effect of medium response on beam propagation we use the Maxwell wave equation.

C. Propagation dynamics

We assume that the control fields are so strong that they are undepleted during propagation and merely acquire phase shifts due to self-phase modulation in the FWM process [5]. So we study only the influence of both linear and nonlinear contributions of polarizations on spatial evolution of the probe and the Stokes beams through the medium. The

paraxial wave equations governing propagation dynamics of probe and Stokes fields can be written in terms of their Rabi frequencies as

$$\frac{\partial g_p}{\partial z} = \frac{i}{2k_p}\left(\frac{\partial^2}{\partial x^2} + \frac{\partial^2}{\partial y^2}\right)g_p + i\eta_p\sigma_{41}\,, \tag{7a}$$

$$\frac{\partial g_s}{\partial z} = \frac{i}{2k_s}\left(\frac{\partial^2}{\partial x^2} + \frac{\partial^2}{\partial y^2}\right)g_s + i\eta_s\sigma_{32}\,, \tag{7b}$$

where $\eta_j(=3\mathcal{N}\lambda_j^2/8\pi)$ are the coupling constants. The first terms in the parentheses on the right-hand sides account for the diffraction. The second terms on the right-hand sides are responsible for the dispersion and absorption or gain of both the probe and Stokes beams. Note that the two propagation equations are coupled via atomic coherences σ_{41} and σ_{32}. The intensity gains for probe and Stokes beam are respectively described by $I_p = |g_p|^2/|g_{p0}|^2$ and $I_s = |g_s|^2/|g_{p0}|^2$, where g_{p0} is the seed signal given on the input of probe beam.

III. RESULTS AND DISCUSSION

We solve the paraxial wave Eqs. (7) using a numerical integration technique based on the split-step fast Fourier transform approach to take into account the diffraction and the integration of the first-order differential equations by the fourth-order Runge-Kutta method to include the source term [42]. In the following, we simulate the coupled Eqs. (7) numerically for different input modes of probe beam as a seed signal and show how intensity and phase profiles are efficiently transferred to the newly generated Stokes beam.

A. Airy beam

Optical Airy beams (ABs) were first discovered by Siviloglou *et al.* in 2007, as a solution of paraxial wave equation in both one and two dimensions [27]. Ideally, an Airy beam contains an infinite energy extended over an infinite space. This makes it impossible to create such a beam physically since it would require an infinite amount of energy. However, the finite-energy Airy beam has been realized in practice by introducing an exponential aperture to truncate the infinite Airy tail. Siviloglou *et al.* experimentally observed the finite-energy one-dimensional (1D) and two-dimensional (2D) Airy beams by imposing a cubic-phase modulation on a broad Gaussian beam in both dimensions [28]. Mathematically, the finite-energy Airy beam is usually obtained by multiplying the Airy function with an exponentially decaying function. In order to demonstrate the frequency conversion, we first choose the probe beam profile as a finite-energy 2D Airy beam. The electric field envelope associated with the finite-energy Airy probe beam at the input facet of the medium ($z = 0$) has the following form:

$$g_p(x, y) = \frac{g_{p0}}{2}\mathrm{Ai}\left(\frac{x}{x_0}\right)\mathrm{Ai}\left(\frac{y}{y_0}\right)\exp\left(a_1\frac{x}{x_0} + a_2\frac{y}{y_0}\right), \tag{8}$$

where g_{p0} is the initial probe amplitude, and $\mathrm{Ai}(x/x_0)$ and $\mathrm{Ai}(y/y_0)$ represent the Airy functions of transverse coordinates x and y normalized by the arbitrary transverse scales x_0 and y_0. The parameters a_1 and a_2 appearing in the exponential function represent the positive quantities. This decay factor truncates the field in both transverse directions and ensures the finite energy of the Airy beam. Figure 2(a) depicts the 2D normalized intensity profile of the finite-energy Airy beam at the entrance of the medium ($z = 0$) for $x_0 = y_0 = 100\,\mu$m and $a_1 = a_2 = 0.1$. Figure 2(b) illustrates 2D normalized intensity of the Airy beam after propagating a distance of $z = 20$ cm in free space. This clearly shows the diffraction-free nature of such a beam. Thus, as expected, the beam maintains its transverse intensity distribution as it propagates in free space. Further, it is also evident from Fig. 2(b) that the Airy beam has accelerated along the 45° axis in the x-y plane. This is so because we have set an equal scaling in the x and y directions. Now, in order to interpret the FWM in an atomic vapor, we propagated the 2D Airy probe beam of Fig. 2(a) through a 5-cm-long medium. Since the Stokes beam is zero at the input, the probe beam is initially absorbed because

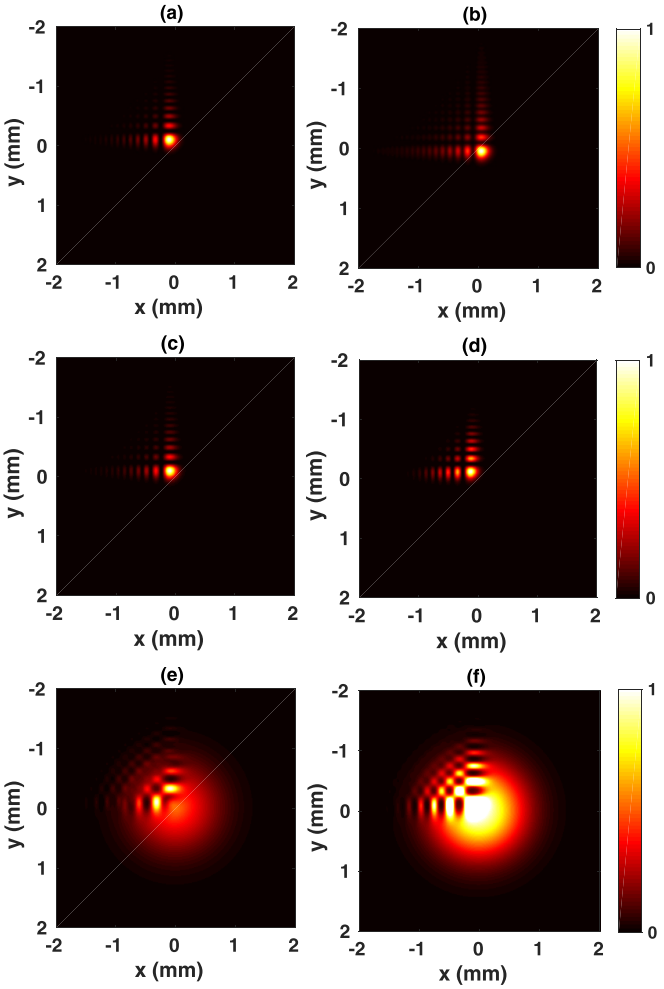

FIG. 2. Normalized intensity profiles of finite energy Airy probe beam (a) at the input $z = 0$ and (b) after propagating $z = 20$ cm in free space. Transmitted profiles of (c) probe beam preserving its original profile and (d) FWM Stokes beam showing identical profile, after traversing $z = 5$-cm-long medium. (e) and (f) Interference patterns of output probe and Stokes beams with a coherent plane wave, respectively. The parameters used are $g_{p0} = 0.01\gamma$, $G_c = 4\gamma$, $\Delta_{c1} = \Delta_{c2} = \Delta_p = \Delta_s = 0$, $\gamma_0 = 0.01\gamma$, $\gamma = 2\pi \times 6$ MHz, $\lambda_p = 780$ nm, $\lambda_s = 795$ nm, and $\mathcal{N} = 1\times10^9$ atoms/cm^3. The input amplitude of the Stokes beam is assumed to be zero.

the linear part dominates over the nonlinear part, which is negligible due to the zero value of the Stokes field. After a short propagation distance, the probe beam resumes its shape due to the generation and parametric amplification by the Stokes field inside the medium. It is interesting to note that the probe is significantly amplified due to its coupling to a new beam created by FWM. Therefore, the gain due to parametric amplification compensates any linear absorption loss of weak probe and Stokes beams at the expense of absorption in strong control fields. The transmitted intensity profile of the probe beam at the exit of the medium is shown in Fig. 2(c). The beam structure is well preserved due to the robustness of such a beam toward the diffraction. Figure 2(d) shows the transmitted intensity profile of the FWM-generated Stokes field. Note that the initial amplitude of the Stokes field was set to zero at the entrance of the medium. However, it is interesting to see that the transverse profile of the probe beam is successfully transferred onto the Stokes beam via the FWM process. We further found that newly generated Airy Stokes beam has started accelerating in a direction opposite to that of probe beam acceleration. These propagation dynamics in FWM medium confirm that the generated Stokes beam is an Airy beam. It is also observed that probe and Stokes beams are significantly amplified due to parametric gain resulting from the FWM process. The integrated intensity gain for the probe and Stokes beam is evaluated to be 1.09 and 1.08, respectively, at the end of the medium. We have further assessed the quality of image transformation by estimating the structural similarity between two output modes, which is about 0.997 [43]. The exact similarity between two transmitted beams reveals the high efficiency of the FWM process. Now, in order to extract the information about transverse phase distribution, we superimpose the output probe and Stokes Airy modes with a copropagating coherent plane wave. The resultant interference patterns are shown in Figs. 2(e) and 2(f) just below the output beams. It should be noted that the multiple high-intensity lobes of an Airy beam are separated by nodal lines (zero intensity) in both the x and y directions. This means that the electric field of an Airy beam undergoes a phase shift of π radians between all adjacent high-intensity lobes. The coherent superposition of such an Airy beam with a plane wave results in alternate maxima and minima intensity distribution as a consequence of constructive and destructive interference, respectively. Any phase conjugation of this interference would result in exchange of maxima and minima position. This is evident when we compare Figs. 2(e) and 2(f). This simply implies that the generated Stokes beam is a conjugate to the probe beam.

B. Bessel beam

Optical Bessel beams (BBs) are diffraction-free light fields whose amplitude is described by a Bessel function of the first kind. Such Bessel function originates as a solution of the HE when written in circular cylindrical coordinates. Theoretically, an ideal Bessel beam contains an infinite number of concentric rings spreading over an infinite area. Thus, it would carry an infinite energy similar to a plane wave, and it is not possible to realize a true Bessel beam with such an infinite energy and extent. However, some suitable approximations have been made to create a Bessel beam experimentally which exhibit the nondiffraction properties over a finite distance and are useful in many optical applications. In practice, Bessel beams of finite energy are produced either by focusing a Gaussian beam with an axicon lens, or by using axisymmetric diffraction gratings, or by placing a narrow annular aperture in the far field. In the year 1987, Durnin *et al.* first theoretically predicted [29] and later experimentally observed [30] the zero-order Bessel beam by illuminating an annular slit placed in the focal plane of a lens. These beams are extremely useful for optical tweezing, particle manipulation, and biomedical imaging [44]. The electric field envelope associated to an ideal Bessel probe beam can be described by

$$g_p(r, \phi, z) = g_{p0} J_n(k_r r) \exp(ik_z z) \exp(\pm in\phi), \tag{9}$$

where $r = \sqrt{x^2 + y^2}$ and J_n is the nth-order Bessel function of the first kind, and k_r and k_z are the radial and longitudinal wave vectors with $k = \sqrt{k_z^2 + k_r^2}$. The parameter k_r determines the effective width of the Bessel beam, and at $k_r = w/c = 2\pi/\lambda$ the central spot assumes its minimum possible diameter. Note that for $k_r = 0$, Eq. (9) reduces to a plane wave. However, for $0 < k_r \leqslant w/c$, it represents a nondiffracting beam as it has same intensity profile $J_0^2(k_r r)$ in every plane normal to direction of propagation. For numerical simulation we have fixed $k_r = 24/\text{mm}$. The transverse intensity distribution for a zero-order ($n = 0$) Bessel beam shows a bright core at the center. The high-order ($n > 0$) Bessel beams have a phase singularity on the beam axis and hence have a dark core at the center. We consider such an axially symmetric finite-energy zero-order Bessel beam to demonstrate the FWM process. We numerically simulated the propagation of a zero-order Bessel beam imprinted initially in the intensity profile of a probe beam through a 5-cm-long medium. Figure 3(a) depicts the normalized intensity distribution of a transmitted Bessel probe beam having a set of concentric rings. The transverse structure of the probe beam is well preserved due to its immunity to optical diffraction. The transmitted intensity profile of frequency-converted Stokes beams is shown in Fig. 3(b). Interestingly, the transmitted profile of the Stokes field has acquired the spatial features identical to that of the probe beam, which signifies the high efficiency of the FWM process. Note that both the probe and Stokes beams have been amplified due to their parametric gain of the FWM process, avoiding any loss due to linear absorption. The integrated intensity gain for both the probe and Stokes beams is close to unity, whereas the structural similarity between transmitted modes is estimated to be about 0.999. Since a Bessel beam is assumed to be made up from plane waves propagating on a cone, one can easily infer that the nodes (null intensity) of the beam correspond to a phase shift of π radians between adjacent rings. This is clearly visible in the phase profiles as depicted in Figs. 3(c) and 3(d) just below their intensity profiles. In order to extract phase information, we superimpose output beams with a copropagating plane wave. This results in an interference pattern with alternate maxima and minima intensity as shown in Figs. 3(e) and 3(f). A careful analysis of these two images suggests that interference fringes are complementary to each other. Thus, we conclude that the generated Stokes beam is a phase conjugate to the probe beam.

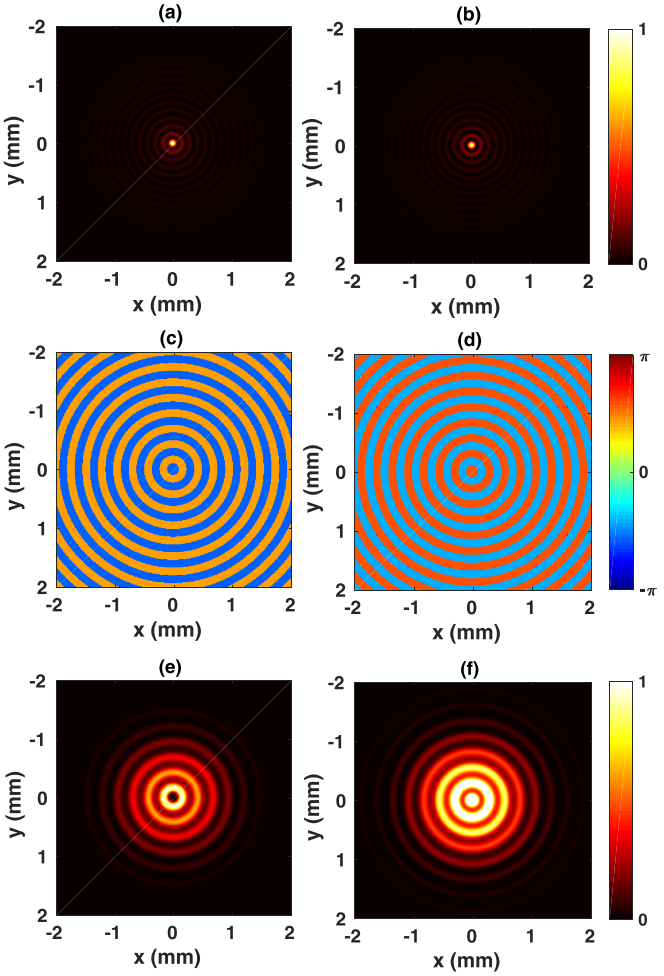

FIG. 3. Normalized intensity distribution of transmitted (a) zero-order Bessel probe beam and (b) converted FWM Stokes beam, (c) and (d) corresponding phase profiles, and (e) and (f) respective interference patterns of these beams with a plane wave. All other parameters are the same as in Fig. 2.

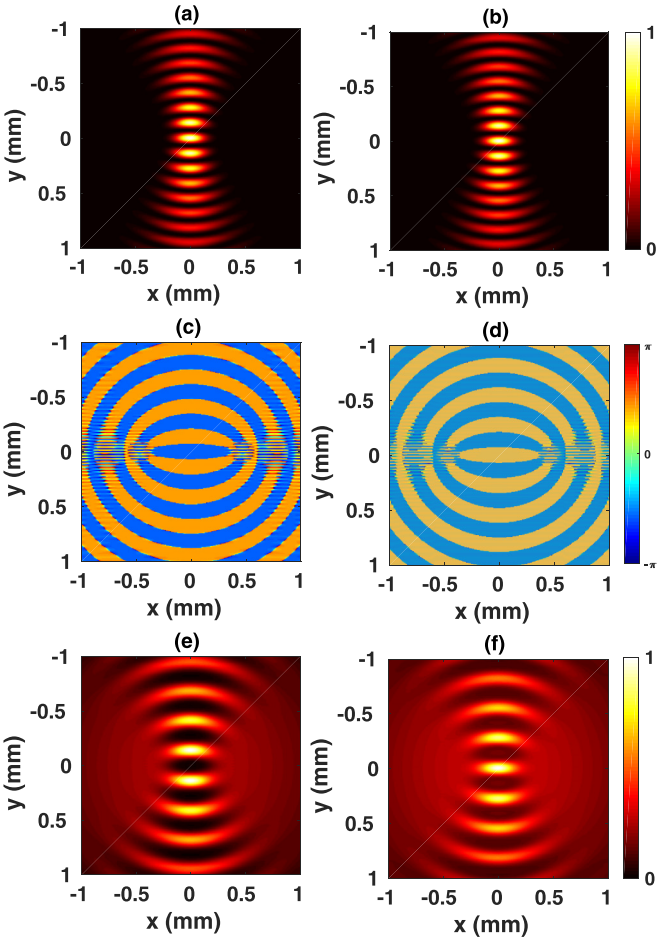

FIG. 4. Normalized intensity distribution of transmitted (a) zero-order Mathieu probe beam and (b) converted FWM Stokes beam, (c) and (d) are the corresponding phase profiles, (e) and (f) show the respective interference patterns of these beams with a plane wave. All other parameters are the same as in Fig. 2.

We further anticipate that a similar concept would apply for higher-order Bessel modes.

C. Mathieu beam

Optical Mathieu beams (MBs) are the most general class of nondiffracting fields whose amplitude is described by the radial and angular Mathieu functions. These functions are solutions of the HE when expressed in the elliptical coordinates system (ξ, η, z). Gutiérrez-Vega *et al.* first theoretically predicted [31] and experimentally demonstrated [45] the zero-order Mathieu beam as a new member of the nondiffracting beam. In their experimental setup they used a thin annular slit modulated by angular Mathieu functions to generate such modes in elliptic coordinates. Mathematically, these modes are described by a product of radial and angular Mathieu functions of order m along with an even (e) and an odd (o) parity. For the sake of simplicity, we consider Mathieu beams with even parity for our FWM analysis as follows:

$$g_p = MB^e_m(\xi, \eta; q) = g_{p0} C_m(q) \mathrm{Je}_m(\xi; q) \mathrm{ce}_m(\eta; q), \quad (10)$$

where $C_m(q)$ $(m = 0, 1, 2, ...)$ is a normalization constant that depends on a dimensionless parameter q. Here, $q = h^2 k_t^2/4$ describes the ellipticity of the elliptic coordinate system with interfocal separation h and transverse wave number $k_t = 2\pi/a$, where a is characteristic beam size. $\mathrm{Je}_m(\xi; q)$ and $\mathrm{ce}_m(\eta; q)$ are mth-order radial and angular even Mathieu functions of the first kind describing the radial and angular distribution of the Mathieu beam, respectively. Here, $\xi \in [0, \infty)$ and $\eta \in [0, 2\pi)$ correspond to radial and angular variables in the elliptical coordinate system. For simplicity in our numerical simulation, we consider the initial probe beam profile as the zero-order Mathieu beam. We choose the parameter of ellipticity $q = 25$ and characteristic structure size $a = 25\,\mu\mathrm{m}$. The numerically propagated transverse profile for the zero-order Mathieu probe beam is shown in Fig. 4(a), whereas the transferred image onto Stokes beams is displayed in Fig. 4(b). These intensity distributions consisting of bright spots along elliptic curves clearly display the elliptical behavior of Mathieu beams. The intensity profiles of transmitted beams are well preserved due to their propagation-invariant nature. Note that this time the nodal lines (or null intensity) are in the form of elliptic lines and correspond to a jump

of π radians phase shift between adjacent bright spots. The phase distributions of both beams are illustrated in Figs. 4(c) and 4(d). The interferograms of superposition of output probe and Stokes modes with a coherent plane wave are shown in Figs. 4(e) and 4(f), respectively. It is evident from the interference fringes that the separate regions of different phases lie on the ellipses. Thus, the characteristics of the elliptic coordinate system are fully reflected in both transverse intensity and phase distributions. Moreover, the interference fringes obtained in two images are complementary to each other, i.e., a maximum corresponds to a minimum and vice versa. A careful visualization of these interference patterns suggests that the generated Stokes beam is a conjugate to the probe beam. A similar concept would apply for higher-order even and odd Mathieu beams. Moreover, the integrated intensity gain for the transmitted probe and Stokes Mathieu beam is estimated to be unity. The structural similarity is approximately 0.998.

D. Weber beam

Optical Weber beams (WBs), also referred to as parabolic beams, are the fourth family of nondiffracting fields. Their spatial structure is described by parabolic cylinder functions. These functions are the exact solutions of the HE written in the parabolic cylindrical coordinate system (ξ, η, z). Bandres *et al.* were the first to demonstrate both theoretically [33] and experimentally [46] the zero-order Weber beam by means of a suitable angular modulation of a thin annular slit. The parabolic coordinates are related to the Cartesian coordinates (x, y, z) by the transformation equations as $x = (\eta^2 - \xi^2)/2$, $y = \eta\xi$, and $z = z$ with domains $\xi \in [0, \infty)$, $\eta \in (-\infty, \infty)$, and $z \in (-\infty, \infty)$. There are two different solutions for the transverse field distributions of Weber beams corresponding to an even and odd parity. However, single Weber beams are defined by products of functions having the same parity in η and ξ. For simplicity in our numerical simulation, we consider only the even Weber beam as follows:

$$g_p = WB_0^e(\xi, \eta; a) = g_{p0}\frac{|\Gamma_1|^2}{\pi\sqrt{2}}\mathrm{P_e}(\sigma\xi; a)\mathrm{P_e}(\sigma\eta; -a), \quad (11)$$

where $\mathrm{P_e}$ is the even real solutions of the parabolic cylinder differential equation. Here, $\sigma = \sqrt{(2k_t)}$ and $\Gamma_1 = \Gamma(1/4 + ia/2)$, where $a \in (-\infty, \infty)$ is a continuous parameter and defines the order of the beam. We consider the fundamental zero-order mode $a = 0$ for the present study. We numerically simulated the propagation of an even zero-order Weber beam imprinted initially in the spatial envelope of the probe beam through a 5-cm-long medium. Figures 5(a) and 5(b) illustrate the normalized intensity profiles of transmitted probe and generated Stokes beams consisting of alternate bright and dark regions along parabolic paths. This clearly shows the parabolic characteristics of Weber beams. It is obvious to see that transverse structures of both beams are identical and preserved during propagation. Note that the intensity patterns are symmetrical about the x and y axes. The nonlinear gain due to parametric amplification compensates any loss by linear absorption. In this case, the integrated intensity gain for the output probe and Stokes Mathieu beam is found to be unity. The structural similarity between the two output modes is nearly equal to 0.999. The transmitted beams also exhibit

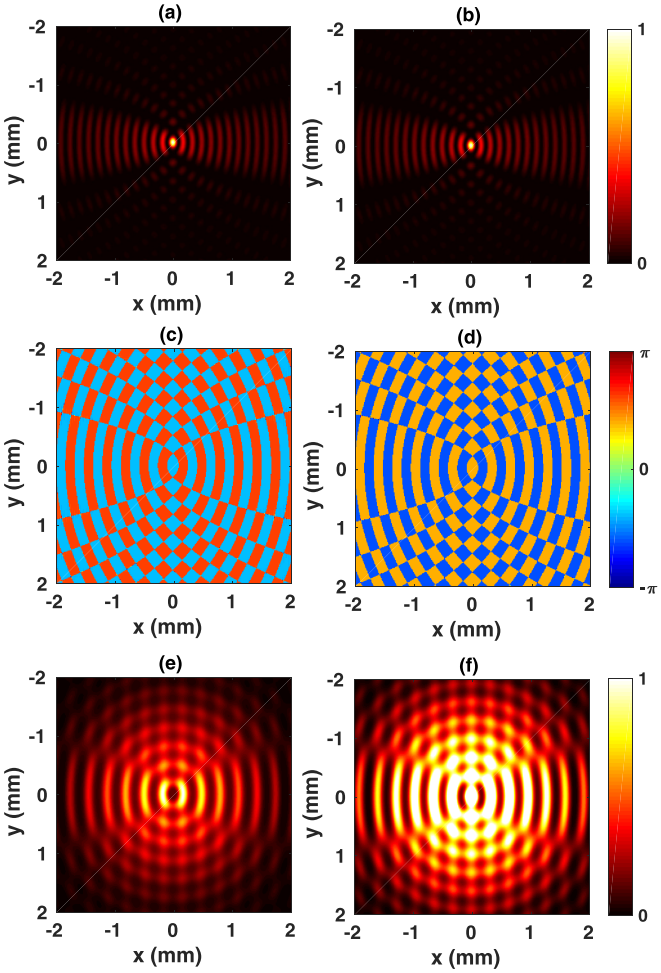

FIG. 5. Normalized intensity distribution of transmitted (a) zero-order Weber probe beam and (b) converted FWM Stokes beam, (c) and (d) corresponding phase profiles, and (e) and (f) respective interference patterns of these beams with a plane wave. All other parameters are the same as in Fig. 2.

well-defined parabolic nodal lines (null intensity). This simply implies that there is a jump of π radians phase shift between adjacent bright spots. This is evident from phase profiles shown in Figs. 5(c) and 5(d). The interference of two output beams with a copropagating plane wave results in alternate maxima and minima intensity distribution. Figures 5(c) and 5(d) depict the fringe patterns. It is noticeable that the resulting fringes are complementary to each other. This implies that both beams are phase conjugate to each other.

IV. CONCLUSION

In conclusion, we have studied the transfer and the nonlinear frequency conversion of different nondiffracting modes based on the FWM process in cold atomic vapor. We have modeled each atom as a four-level double-Λ type atomic system where two strong control fields and a weak probe field mutually interact to produce a low frequency weak Stokes field. We have found that an arbitrary mode such as Airy, Bessel, Mathieu, and Weber beams imprinted initially in the envelope of the probe beam is preserved and successfully

transferred to the generated Stokes field after propagation through medium. We have further used the interferometry technique to confirm that the phase profiles of the frequency converted Stokes beam are phase conjugate to that of the transmitted probe beam. It is also observed that any loss due to linear absorption is compensated by parametric amplification. The structural similarity between two transmitted images is estimated to be about 99%, indicating the high success and efficiency of the nonlinear FWM process.

ACKNOWLEDGMENT

O.N.V. gratefully acknowledges the financial support from the UGC Government of India for funding this research work through a D.S. Kothari Postdoctoral Fellowship with Grant No. F.4-2/2006(BSR)/PH/20-21/0054.

APPENDIX: COEFFICIENTS FOR POLARIZATIONS

$$\alpha_p = \frac{-i|G_c|^2}{D}\left[\left(\frac{\Gamma_{21}+\Gamma_{43}}{\Gamma_{23}}+\frac{\Gamma_{21}\Gamma_{43}}{|G_c|^2}\right)N_{14} - \frac{\Gamma_{21}N_{13}}{\Gamma_{31}}-\frac{\Gamma_{43}N_{24}}{\Gamma_{24}}\right]\Gamma_{23} \quad \text{(A1)}$$

$$\beta_p = \frac{-iG_c^2}{D}\left[\frac{\Gamma_{21}+\Gamma_{43}}{\Gamma_{23}}N_{23}-\frac{\Gamma_{43}}{\Gamma_{31}}N_{13}+\frac{\Gamma_{21}}{\Gamma_{42}}N_{24}\right]\Gamma_{23} \quad \text{(A2)}$$

$$\alpha_s = \frac{i|G_c|^2}{D^*}\left[\left(\frac{\Gamma_{12}+\Gamma_{34}}{\Gamma_{14}}+\frac{\Gamma_{12}\Gamma_{34}}{|G_c|^2}\right)N_{23} + \frac{\Gamma_{34}N_{13}}{\Gamma_{13}}-\frac{\Gamma_{12}N_{24}}{\Gamma_{24}}\right]\Gamma_{14} \quad \text{(A3)}$$

$$\beta_s = \frac{-iG_c^2}{D^*}\left[\frac{\Gamma_{12}+\Gamma_{34}}{\Gamma_{14}}N_{14}+\frac{\Gamma_{12}}{\Gamma_{31}}N_{13}+\frac{\Gamma_{34}}{\Gamma_{42}}N_{24}\right]\Gamma_{14}, \quad \text{(A4)}$$

with

$$D = \Gamma_{21}\Gamma_{23}\Gamma_{41}\Gamma_{43} + |G_c|^2(\Gamma_{23}+\Gamma_{41})(\Gamma_{21}+\Gamma_{43})$$

$$N_{13} = N_{14} = \frac{|\Gamma_{31}|^2}{4|G_c|^2+|\Gamma_{31}|^2+|\Gamma_{42}|^2}$$

$$N_{23} = N_{24} = \frac{|\Gamma_{42}|^2}{4|G_c|^2+|\Gamma_{31}|^2+|\Gamma_{42}|^2},$$

where the complex decay rates are defined as $\Gamma_{21} = \gamma_{21}^c + i(\Delta_p - \Delta_{c1}) = \Gamma_{12}^*$, $\Gamma_{31} = [\gamma_{31}+\gamma_{32}+i\Delta_{c2}] = \Gamma_{13}^*$, $\Gamma_{32} = [\gamma_{31}+\gamma_{32}+i\Delta_s] = \Gamma_{23}^*$, $\Gamma_{41} = [\gamma_{41}+\gamma_{42}+i\Delta_p] = \Gamma_{14}^*$, $\Gamma_{42} = [\gamma_{41}+\gamma_{42}+i\Delta_{c1}] = \Gamma_{24}^*$, and $\Gamma_{43} = [\gamma_{41}+\gamma_{42}+\gamma_{31}+\gamma_{32}+i(\Delta_p-\Delta_{c2})] = \Gamma_{34}^*$. Here, $\Delta_p = \omega_{41}-\omega_p$, $\Delta_s = \omega_{32}-\omega_s$, $\Delta_{c1} = \omega_{31}-\omega_{c2}$, and $\Delta_{c2} = \omega_{42}-\omega_{c1}$ are respective single-photon detunings. γ_{jk} are the radiative decay rates from the state $|j\rangle$ to $|k\rangle$ and are treated to be equal: $\gamma_{31} = \gamma_{32} = \gamma_{41} = \gamma_{42} = \gamma/2$. The dipole dephasing rate due to collisions is assumed to be zero ($\gamma_{jk\neq 21}^c = 0$) except ground state coherence: $\gamma_{21}^c = \gamma_0$. To simplify the expressions, we have assumed that $G_{c1} = G_{c2} = G_c$.

[1] A. J. Merriam, S. J. Sharpe, M. Shverdin, D. Manuszak, G. Y. Yin, and S. E. Harris, Efficient nonlinear frequency conversion in an all-resonant double-Λ system, Phys. Rev. Lett. **84**, 5308 (2000).

[2] C. H. van der Wal, M. D. Eisaman, A. André, R. L. Walsworth, D. F. Phillips, A. S. Zibrov, and M. D. Lukin, Atomic memory for correlated photon states, Science **301**, 196 (2003).

[3] Q.-F. Chen, B.-S. Shi, Y.-S. Zhang, and G.-C. Guo, Entanglement of the orbital angular momentum states of the photon pairs generated in a hot atomic ensemble, Phys. Rev. A **78**, 053810 (2008).

[4] V. Boyer, A. M. Marino, and P. D. Lett, Generation of spatially broadband twin beams for quantum imaging, Phys. Rev. Lett. **100**, 143601 (2008).

[5] R. W. Boyd, *Nonlinear Optics*, 3rd ed. (Academic, New York, 2008).

[6] S. E. Harris, J. E. Field, and A. Imamoğlu, Nonlinear optical processes using electromagnetically induced transparency, Phys. Rev. Lett. **64**, 1107 (1990).

[7] S. P. Tewari and G. S. Agarwal, Vacuum-ultraviolet generation using electromagnetic-field-induced transparency, Phys. Rev. Lett. **66**, 1797 (1991).

[8] X. Liu, B. Kuyken, G. Roelkens, R. Baets, R. M. Osgood, and W. M. J. Green, Bridging the mid-infrared-to-telecom gap with silicon nanophotonic spectral translation, Nat. Photon. **6**, 667 (2012).

[9] P. H. Souto Ribeiro, S. Pádua, and C. H. Monken, Image and coherence transfer in the stimulated down-conversion process, Phys. Rev. A **60**, 5074 (1999).

[10] P. H. Souto Ribeiro, D. P. Caetano, M. P. Almeida, J. A. Huguenin, B. Coutinho dos Santos, and A. Z. Khoury, Observation of image transfer and phase conjugation in stimulated down-conversion, Phys. Rev. Lett. **87**, 133602 (2001).

[11] D.-S. Ding, Z.-Y. Zhou, W. Huang, B.-S. Shi, X.-B. Zou, and G.-C. Guo, Experimental up-conversion of images, Phys. Rev. A **86**, 033803 (2012).

[12] G. Walker, A. S. Arnold, and S. Franke-Arnold, Trans-spectral orbital angular momentum transfer via four-wave mixing in Rb vapor, Phys. Rev. Lett. **108**, 243601 (2012).

[13] O. N. Verma, R. K. Pandey, R. R. Yadav, and A. Patel, Efficient transfer of spatial intensity and phase information of arbitrary modes via four-wave mixing in an atomic vapor, Phys. Rev. A **106**, 053713 (2022).

[14] J. W. R. Tabosa and D. V. Petrov, Optical pumping of orbital angular momentum of light in cold cesium atoms, Phys. Rev. Lett. **83**, 4967 (1999).

[15] A. M. Akulshin, R. J. McLean, E. E. Mikhailov, and I. Novikova, Distinguishing nonlinear processes in atomic media via orbital angular momentum transfer, Opt. Lett. **40**, 1109 (2015).

[16] A. M. Akulshin, D. Budker, and R. J. McLean, Parametric wave mixing enhanced by velocity-insensitive two-photon excitation in Rb vapor, J. Opt. Soc. Am. B **34**, 1016 (2017).
[17] A. Chopinaud, M. Jacquey, B. Viaris de Lesegno, and L. Pruvost, High helicity vortex conversion in a rubidium vapor, Phys. Rev. A **97**, 063806 (2018).
[18] N. Prajapati, A. M. Akulshin, and I. Novikova, Comparison of collimated blue-light generation in ^{85}Rb atoms via the D_1 and D_2 lines, J. Opt. Soc. Am. B **35**, 1133 (2018).
[19] N. S. Mallick and T. N. Dey, Four-wave mixing-based orbital angular momentum translation, J. Opt. Soc. Am. B **37**, 1857 (2020).
[20] J. Qiu, Z. Wang, D. Ding, Z. Huang, and B. Yu, Control of space-dependent four-wave mixing in a four-level atomic system, Phys. Rev. A **102**, 033516 (2020).
[21] C. Yu and Z. Wang, Engineering helical phase via four-wave mixing in the ultraslow propagation regime, Phys. Rev. A **103**, 013518 (2021).
[22] M. Jain, H. Xia, G. Y. Yin, A. J. Merriam, and S. E. Harris, Efficient nonlinear frequency conversion with maximal atomic coherence, Phys. Rev. Lett. **77**, 4326 (1996).
[23] D. Bortman-Arbiv, A. D. Wilson-Gordon, and H. Friedmann, Effect of four-wave mixing on induced waveguiding, Phys. Rev. A **61**, 033806 (2000).
[24] L. Zhang and J. Evers, Diffractionless image propagation and frequency conversion via four-wave mixing exploiting the thermal motion of atoms, Phys. Rev. A **89**, 013817 (2014).
[25] H. Shpaisman, A. D. Wilson-Gordon, and H. Friedmann, Electromagnetically induced waveguiding in double-Λ systems, Phys. Rev. A **71**, 043812 (2005).
[26] M. V. Berry and N. L. Balazs, Nonspreading wave packets, Am. J. Phys. **47**, 264 (1979).
[27] G. A. Siviloglou and D. N. Christodoulides, Accelerating finite energy airy beams, Opt. Lett. **32**, 979 (2007).
[28] G. A. Siviloglou, J. Broky, A. Dogariu, and D. N. Christodoulides, Observation of accelerating Airy beams, Phys. Rev. Lett. **99**, 213901 (2007).
[29] J. Durnin, Exact solutions for nondiffracting beams. I. The scalar theory, J. Opt. Soc. Am. A **4**, 651 (1987).
[30] J. Durnin, J. J. Miceli, and J. H. Eberly, Diffraction-free beams, Phys. Rev. Lett. **58**, 1499 (1987).
[31] J. C. Gutiérrez-Vega, M. D. Iturbe-Castillo, and S. Chávez-Cerda, Alternative formulation for invariant optical fields: Mathieu beams, Opt. Lett. **25**, 1493 (2000).
[32] P. Zhang, Y. Hu, T. Li, D. Cannan, X. Yin, R. Morandotti, Z. Chen, and X. Zhang, Nonparaxial Mathieu and Weber accelerating beams, Phys. Rev. Lett. **109**, 193901 (2012).
[33] M. A. Bandres, J. C. Gutiérrez-Vega, and S. Chávez-Cerda, Parabolic nondiffracting optical wave fields, Opt. Lett. **29**, 44 (2004).
[34] M. A. Bandres and B. M. Rodríguez-Lara, Nondiffracting accelerating waves: Weber waves and parabolic momentum, New J. Phys. **15**, 013054 (2013).
[35] D. Wei, Y. Yu, M. Cao, L. Zhang, F. Ye, W. Guo, S. Zhang, H. Gao, and F. Li, Generation of Airy beams by four-wave mixing in Rubidium vapor cell, Opt. Lett. **39**, 4557 (2014).
[36] J. Baumgartl, M. Mazilu, and K. Dholakia, Optically mediated particle clearing using Airy wavepackets, Nat. Photon. **2**, 675 (2008).
[37] P. Polynkin, M. Kolesik, J. V. Moloney, G. A. Siviloglou, and D. N. Christodoulides, Curved plasma channel generation using ultraintense Airy beams, Science **324**, 229 (2009).
[38] T. Vettenburg, H. I. C. Dalgarno, J. Nylk, C. Coll-Lladó, D. E. K. Ferrier, T. Čižmár, F. J. Gunn-Moore, and K. Dholakia, Light-sheet microscopy using an Airy beam, Nat. Methods **11**, 541 (2014).
[39] D. Abdollahpour, S. Suntsov, D. G. Papazoglou, and S. Tzortzakis, Spatiotemporal Airy light bullets in the linear and nonlinear regimes, Phys. Rev. Lett. **105**, 253901 (2010).
[40] V. Balić, D. A. Braje, P. Kolchin, G. Y. Yin, and S. E. Harris, Generation of paired photons with controllable waveforms, Phys. Rev. Lett. **94**, 183601 (2005).
[41] M. D. Lukin, P. R. Hemmer, M. Löffler, and M. O. Scully, Resonant enhancement of parametric processes via radiative interference and induced coherence, Phys. Rev. Lett. **81**, 2675 (1998).
[42] G. P. Agrawal, *Nonlinear Fiber Optics*, 3rd ed. (Academic, New York, 2001).
[43] Z. Wang, A. Bovik, H. Sheikh, and E. Simoncelli, Image quality assessment: From error visibility to structural similarity, IEEE Trans. Image Process. **13**, 600 (2004).
[44] D. McGloin and K. Dholakia, Bessel beams: Diffraction in a new light, Contemp. Phys. **46**, 15 (2005).
[45] J. C. Gutiérrez-Vega, M.D. Iturbe-Castillo , G.A. Ramírez, E. Tepichín, R. Rodríguez-Dagnino, S. Chávez-Cerda, and G.H.C. New, Experimental demonstration of optical Mathieu beams, Opt. Commun. **195**, 35 (2001).
[46] C. López-Mariscal, M. A. Bandres, J. C. Gutiérrez-Vega, and S. Chávez-Cerda, Observation of parabolic nondiffracting optical fields, Opt. Express **13**, 2364 (2005).